Nonlinear Analysis for Stabilization of Interchange mode in LHD Plasmas

K.Ichiguchi, N.Nakajima, B.A.Carreras[A]

National Institute for Fusion Science, Oroshi-cho 322-6, Toki 509-5292, Japan

Oak Ridge National Laboratory, Oak Ridge, Tennessee 37831, USA[A]

Abstract

The nonlinear behavior of the interchange mode in the LHD plasma depends on the overlap of the vortices with different helicity. If the vortices are separated in the radial direction, each mode saturates mildly with generating the local flat regions in the pressure profile. In the case of the significant overlap of the vortices, appearance of large scale convection results in sudden global reduction of the pressure. Sequence of the saturated pressure profile in the increase of beta can suppress the overlap. Self-organization of the pressure profile to suppress the overlap of the vortices can be the stabilizing mechanism in the LHD plasma.

1 Introduction

In the Large Helical Device (LHD), the average beta value of $\langle\beta\rangle = 3.2\%$ was successfully achieved in the configuration with the inward shift of the vacuum magnetic axis[1]. In order to study the magnetohydrodynamic (MHD) stability of the LHD plasma, the linear theory was applied assuming a smooth pressure profile at first. Figure 1 shows the Mercier unstable region[2] for the pressure profile of

$$P = P_0(1-\rho^2)(1-\rho^8). \tag{1}$$

This profile is consistent with the experimental results for the Shafranov shift at low beta[3]. The beta value at the magnetic axis is roughly scaled as $\beta_0 \simeq (1/2)\langle\beta\rangle$ for this pressure profile. This figure shows the core region is quite unstable for $\langle\beta\rangle < 1.5\%$. Also, the linear analysis by using the RESORM code[4] showed that the low n ideal interchange modes resonant at the Mercier unstable region are linearly unstable[5], where n denotes the toroidal mode number.

To explain the discrepancy between theory and experiment it is necessary to invoke the existence of a stabilizing mechanism. The iteration of equilibrium calculation with the VMEC code[6] and the linear stability analysis with the RESORM code showed that the local flattening of the pressure profile effectively stabilizes the interchange mode[7]. The resultant pressure profile stable for low n ideal modes is staircase like. However, it was not clear whether such profile can be generated automatically or what happens in the case of the mode overlapping. In order to solve these problems, it is necessary to examine the nonlinear behavior of multi-helicity interchange modes. For this purpose, we developed a nonlinear code called NORM based on the reduced MHD equations[8].

The NORM code was applied to low beta LHD plasmas which are linearly unstable to the ideal interchange modes[8]. In the case of $\beta_0 = 0.5\%$ with the pressure profile of eq.(1), the kinetic energy of the perturbation is mildly saturated. The modes with different helicity interact indirectly only through the local variation of the pressure profile. As a result, a staircase like pressure profile is generated as was predicted by the linear calculations[7]. In the case of $\beta_0 = 1.0\%$ with the same pressure profile, a bursting activity occurs in the kinetic energy, which causes a significant reduction of the pressure. However, if the pressure profile saturated at $\beta_0 = 0.5\%$ is used for the initial profile, the bursting activity can be suppressed. Thus, it was indicated that the continuous deformation of the pressure profile due to the nonlinear evolution of the interchange mode may be the stabilizing mechanism in the LHD plasmas.

In the present study, we make a progress of the nonlinear study by increasing the beta value up to $\beta_0 = 1.5\%$ and confirm that the stabilizing mechanism in the LHD plasma is attributed to the deformation of the pressure profile. In our numerical calculations, we consider the nonlinear evolution of low k interchange modes, where k denotes the wave number. The effect of the high k resistive interchange modes on those low k modes is through effective dissipation terms. The renormalized theory of resistive interchange modes shows that the turbulence-induced viscosity and heat conductivity depend linearly with beta[9]. Here we include this effect by multiplying a factor to the values used in Ref.[8] depending on the beta value. The increase of the viscosity and the heat conductivity reduces the low k growth rate of the interchange mode and broadens the eigenfunctions in the radial direction[9, 10]. Here we study the nonlinear behavior of $\beta_0 = 1.0\%$ and 1.5% equilibria with slight increase of the dissipation. We also discuss the effect of the self-consistent poloidal flow at $\beta_0 = 0.5\%$.

2 Basic Equations and Numerical Configurations

The NORM code solves the reduced MHD equations composed of Ohm's law, vorticity equation, and equation of state. These equations can be written in terms of the poloidal magnetic flux, Ψ, the velocity stream function, Φ, and the plasma pressure, P. The normalized equations are:

$$\frac{\partial \Psi}{\partial t} = -\left(\frac{R}{R_0}\right)^2 \mathbf{B}\cdot\nabla\Phi + \frac{1}{S}J_\zeta, \tag{2}$$

$$\frac{dU}{dt} = \left(\frac{R}{R_0}\right)^2 \left(-\mathbf{B}\cdot\nabla J_\zeta + \frac{\beta_0}{2\varepsilon^2}\nabla\Omega\times\nabla P\cdot\nabla\zeta\right) + \nu\hat{\nabla}_\perp^2 U, \tag{3}$$

and

$$\frac{dP}{dt} = \kappa_\perp \Delta_* P + \varepsilon^2 \kappa_\parallel \left(\frac{R}{R_0}\right)^2 \mathbf{B}\cdot\nabla(\mathbf{B}\cdot\nabla P). \tag{4}$$

Here, ζ denotes the toroidal angle and $\nabla_\perp$ is defined as $\nabla_\perp = \nabla - \nabla\zeta(\partial/\partial\zeta)$. The magnetic differential operator and the convective time derivative are given by

$$\mathbf{B}\cdot\nabla = g\left(\frac{R_0}{R}\right)^2 \frac{\partial}{\partial\zeta} - \nabla\Psi\times\nabla\zeta\cdot\nabla \tag{5}$$

and

$$\frac{d}{dt} = \frac{\partial}{\partial t} + \mathbf{v}_\perp\cdot\nabla, \quad \mathbf{v}_\perp = \left(\frac{R}{R_0}\right)^2 \nabla\Phi\times\nabla\zeta, \tag{6}$$

respectively. The factor g implies the diamagnetic effect in the toroidal field and the term of $\nabla\Omega$ means the averaged magnetic curvature driving the interchange mode. The vorticity U and the toroidal current density J_ζ are expressed by

$$U = \hat{\nabla}_\perp^2 \Phi = \left(\frac{R}{R_0}\right)^2 \nabla \cdot \nabla_\perp \Phi, \quad \text{and} \quad J_\zeta = \Delta_* \Psi = \left(\frac{R}{R_0}\right)^2 \nabla \cdot \left(\frac{R_0}{R}\right)^2 \nabla_\perp \Psi, \tag{7}$$

respectively. Here β_0 and S denote the beta value at the axis and the magnetic Reynolds number, respectively. The inverse aspect ratio ε is given by a/R_0 with the major radius R_0 and the average minor radius a. The time is normalized by the poloidal Alfvén time τ_A. Viscosity, perpendicular and parallel heat conductivity terms are introduced with the coefficients of ν, $\kappa_\perp$ and $\kappa_\parallel$, respectively. In the resistivity and the heat conductivity terms , only the perturbed parts of J_ζ and P are included, respectively.

The flux coordinates (ρ, θ, ζ) are employed to simplify the magnetic differential operator. Here ρ and θ are the square root of the normalized toroidal flux and the poloidal angle, respectively. The details of the NORM code are explained in Ref.[8]. This code uses a three-dimensional static equilibrium which is calculated by the VMEC code[6]. The zero net-current equilibria for the shifted-in LHD configuration ($R_{ax} = 3.6$m) under the free boundary condition[11] are examined in the present study.

For the nonlinear analysis, the resistivity is fixed to $S = 10^6$. Other dissipation parameters are given as $(\nu, \kappa_\perp, \kappa_\parallel) = F_\beta(\nu_0, \kappa_{\perp 0}, \kappa_{\parallel 0})$. Here, $\nu_0 = 10^{-4}$, $\kappa_{\perp 0} = 10^{-6}$ and $\varepsilon^2 \kappa_{\parallel 0} = 10^{-2}$ ($\varepsilon = 0.16$), which are the same as used in Ref.[8]. The factor F_β is chosen as $F_\beta = 1.26$ and 1.64 for $\beta_0 = 1.0\%$ and 1.5%, respectively. The linear growth rates with these parameters at $\beta_0 = 0.5\%$, 1.0% and 1.5% are shown in Fig.2 as the function of the toroidal mode number n. All unstable modes have typical interchange mode structure. The structure of the eigenfunction is a little broader than that of the corresponding ideal mode. The growth rates at $\beta_0 = 1.0\%$ and 1.5% are much larger than those at 0.5%. The growth rates at $\beta_0 = 1.5\%$ are reduced to the values similar to those at $\beta_0 = 1.0\%$ because of the increase of F_β.

3 Bursting Behavior with Mode Overlapping

We study the nonlinear behavior of the interchange mode with multi-helicity. The perturbations are assumed to be expanded in the Fourier series as follows:

$$\tilde{\Psi} = \sum_{mn} \tilde{\Psi}_{mn}(\rho)\cos(m\theta - n\zeta), \quad \tilde{\Phi} = \sum_{mn} \tilde{\Phi}_{mn}(\rho)\sin(m\theta - n\zeta), \quad \tilde{P} = \sum_{mn} \tilde{P}_{mn}(\rho)\cos(m\theta - n\zeta), \tag{8}$$

where m and n are the poloidal and the toroidal mode numbers, respectively. It was obtained the perturbations in the equilibrium with the pressure profile of eq.(1) at $\beta_0 = 0.5\%$ with $F_\beta = 1.0$ is saturated mildly[8].

Here, we examine the nonlinear evolution of the instability in the equilibrium with the same pressure profile of eq.(1) at $\beta_0 = 1.0\%$ with $F_\beta = 1.26$. The calculations are carried out for the modes shown in Fig.3. The modes are selected so as to cover all of the resonant space in the region of $1/3 \leq \iota \leq 1$ for $0 \leq n \leq 7$. Figure 4 shows the time evolution of the kinetic energy, which is defined by $E_k = \sum_n E_k^n$, $E_k^n = \frac{1}{2}\int |\nabla_\perp \sum_m \tilde{\Phi}_{mn}\sin(m\theta - n\zeta)|^2 dV$. The $(m,n) = (5,2)$ mode is dominant in the linear phase as shown in Fig.2. After the nonlinear saturation of the dominant mode, a bursting activity appears. In the period of of $4300\tau_A \leq t \leq 6500\tau_A$, many modes are excited simultaneously. In order to see what happens in the bursting period, we plot the stream lines as shown in Fig.5. Before the bursting phenomena, at $t = 4300\tau_A$, the modes with $(m,n) = (4,2)$ and $(m,n) = (5,2)$ are localized around the rational surfaces with $\iota = 1/2$ and 2/5 separately as shown in Fig.5(a). The bursting activity is triggered at $t = 4400\tau_A$. As shown in Fig.5(b), the absolute value of the stream function corresponding to the $(m,n) = (7,3)$ mode becomes comparable to those of the $(4,2)$ and $(5,2)$ modes. Furthermore, the vortices with different helicity starts to merge each other at this time. At $t = 4620\tau_A$, where the kinetic energy has the maximum value, the vortices are strongly overlapped as shown in Fig.5(c). The size of a singly vortex becomes much larger than that before the bursting activity. In the vortex merging, the free energy due to the pressure gradient is abruptly released in the wide range of the radial direction. Then, the kinetic energy shows the busting behavior.

The large size vortex transports the core pressure to the peripheral region by the convection. As a result, the average pressure in the wide core region degrades just after the bursting phenomena ($t = 6500\tau_A$) as shown in Fig.6, where the average pressure is defined as $\langle P \rangle = P_{eq} + \tilde{P}_{00}$. The subscript '$eq$' denotes the equilibrium quantity. In the saturated phase at $t = 27000$, the pressure is substantially reduced in the large core region of $\rho \leq 0.5$. Therefore,

the bursting activity may correspond to the internal disruption and it may limit the achievable beta.

In the peripheral region for $\rho > 0.7$, any significant activity is not observed. This is because the driving force of the interchange mode is localized in the region of $\rho < 0.5$ for this equilibrium, as shown in Fig.1. The pressure is increased a little in the peripheral region because the bursting activity in the core region convects the pressure. The average rotational transform defined by $\langle \iota \rangle = (1/\rho)(\partial \tilde{\Psi}_{00}/\partial \rho) + \iota_{eq}$ is also plotted in Fig.6. The nonlinear effect on the average rotational transform is much weaker than on the pressure. These results are quite similar to the result for $F_\beta = 1.0$[8].

4 Sequence of equilibria with nonlinearly saturated profiles

The bursting activity is obtained under the assumption that the pressure profile is fixed to the profile of eq.(1). In the actual experiment, the pressure profile changes continuously as the beta increases. In order to simulate this situation, we consider a sequence of equilibria at different beta values. Each equilibrium of this sequence is calculated by using the pressure profile of the saturated nonlinear state of the previous beta value. In Fig.7, the line for $t = 0\tau_A$ corresponds to the pressure profile obtained in the nonlinear saturated state for $\beta_0 = 0.5\%$[8]. We use this profile to calculate a $\beta_0 = 1.0\%$ equilibrium, which is then used as initial condition for the dynamical evolution of the interchange instabilities. The profile is locally flattened at the surfaces corresponding to ι =2/5, 3/7 and 1/2. This is because the single modes with $(m,n) = (5,2)$, (7,3) and (2,1) were saturated separately at $\beta_0 = 0.5\%$. The local flattening of the pressure profile reduces the driving force of the interchange mode. Figure 8 shows the linear growth rates at $\beta_0 = 1.0\%$ for the saturated pressure profile. The growth rates for the fixed pressure profile of eq.(1) are also plotted for comparison. The linear growth rates for n =1, 2 and 4 are decreased due to the local flattening of the pressure profile.

Figure 9 shows the time evolution of the kinetic energy with $F_\beta = 1.26$ at $\beta_0 = 1.0\%$ for the pressure profile saturated at $\beta_0 = 0.5\%$. The dominant linear mode is $(m,n) = (8,3)$ mode. After the saturation of the the dominant linear mode, the variation of the kinetic energy is small and slow in the nonlinear phase. Only one burst is seen around $t = 21500\tau_A$ in the time evolution. The stream lines at this time are plotted in Fig.10. The vortices with different helicity are almost separated in the radial direction. The flow of the vortices flattens the pressure profile

locally around the surfaces with $\iota = 1/2$, 3/5 and 2/3 as shown in Fig.7. This means that there is no significant pressure reduction in the wide region over the multiple low order rational surfaces. These properties are different from those in the bursting case with the fixed initial pressure profile. Furthermore, the pressure profile is deformed gradually in the time evolution. The reduction of the pressure at the final state ($t = 27000$) is much smaller than that in the bursting case. Therefore, the beta value of $\beta_0 = 1.0\%$ can be achieved without the bursting activity by the deformation of the initial pressure profile.

Next, we examine the case of $\beta_0 = 1.5\%$ for $F_\beta = 1.64$. In this case, we utilize the pressure profile saturated at $\beta_0 = 1.0\%$ for the initial profile in the $\beta_0 = 1.5\%$ calculation, which is shown by the solid line for $t = 27000\tau_A$ in Fig.7. Figure 11 shows the time evolution of the kinetic energy of the perturbations. The behavior of the total kinetic energy is quite mild in the nonlinear phase. In this time evolution, the dominant linear mode is $(m,n) = (5,2)$ mode. The saturation of this mode results in the enhancement of the local flattening of the pressure around the $\iota = 2/5$. Simultaneously, the pressure gradient around the surface with $\iota = 6/11$ and 6/10 is also enhanced. Then, the $n = 6$ mode that is resonant at these surfaces is slowly excited and dominates the nonlinear saturation. In this case, the driving force of the $(m,n) = (5,2)$ is already reduced by the deformation of the initial pressure profile. Therefore, the enhancement of the pressure gradient is weak. This suppresses the abrupt excitation of simultaneous multiple modes, unlike the bursting case. Figure 12 shows the pressure contour at $t = 27000\tau_A$. We can observe not only the poloidally averaged flattening structure but also fine deformation in the poloidal direction corresponding to the saturated mode at each resonant surface. The formation of such structure can be considered as a self-organization of the plasma in the nonlinear evolution of the interchange mode. On the contrary, as is also shown in Fig.11, a tremendous bursting activity occurs if we fix the initial pressure profile to eq.(1).

These results indicates that the continuous deformation of the pressure profile due to the nonlinear saturation interchange mode can be the stabilizing mechanism in the beta ramp-up of the LHD plasma. This deformation of the pressure profile is a continuous self-organization, which can provide a stable path to the high beta regime for the LHD plasma.

5 Properties of Saturated Pressure and Effects of Self-Consistent Flow

It is interesting to examine the properties of the nonlinearly saturated pressure profiles obtained in the pressure sequence procedure. Figure 13 shows the pressure profiles saturated at $\beta_0 = 0.5\%$[8], 1.0% and 1.5% in the nonlinear evolution. As a local structure, all of them are locally flattened at the rational surfaces. The flattening regions result from the exhaustion of the driving force by the resonant modes. Figure 14 shows the profile of the Mercier quantity D_I[2] of the no net current equilibria which are calculated with the saturated pressure profiles. The local stable regions are seen at the low order rational surfaces, for example, the surfaces of $\iota = 2/5$, 1/2 and 2/3, which correspond to the local pressure flattening regions.

As for the change of the global structure, the pressure profile is broadened gradually as the beta value is increased. Figure 15 shows the comparison of the peaking factor defined by $\beta_0/\langle\beta\rangle$ between the numerical and the experimental results[12]. The tendency of broadening of the saturated pressure profile is quite consistent with the experimental results.

We also study the effects of uniform poloidal flow induced self-consistently by the interchange mode. For this purpose, we use the Fourier expansion for the perturbations,

$\tilde{\Psi} = \sum_{mn}[\tilde{\Psi}^c_{mn}(\rho)\cos(m\theta - n\zeta) + \tilde{\Psi}^s_{mn}(\rho)\sin(m\theta - n\zeta)]$,

$\tilde{\Phi} = \sum_{mn}[\tilde{\Phi}^c_{mn}(\rho)\cos(m\theta - n\zeta) + \tilde{\Phi}^s_{mn}(\rho)\sin(m\theta - n\zeta)]$

and $\tilde{P} = \sum_{mn}[\tilde{P}^c_{mn}(\rho)\cos(m\theta - n\zeta) + \tilde{P}^s_{mn}(\rho)\sin(m\theta - n\zeta)]$,

instead of eq.(8). In above expression, $\tilde{\Phi}^c_{00}$ component corresponds to the uniform poloidal flow. Figure 16 shows the time evolution of the kinetic energy for the equilibrium with the pressure profile of eq.(1) at $\beta_0 = 0.5\%$ for $F_\beta = 1.0$. In this case, the toroidal component of the kinetic energy is calculated as $E^n_k = \frac{1}{2}\int |\nabla_\perp \sum_m[\tilde{\Phi}^c_{mn}\cos(m\theta - n\zeta) + \tilde{\Phi}^s_{mn}\sin(m\theta - n\zeta)]|^2 dV$. The $n = 0$ component E^0_k grows significantly in the nonlinear phase and becomes almost dominant for $t \geq 20000\tau_A$. This result implies the resistive interchange mode can generate uniform poloidal flow self-consistently in the toroidal geometry. Figure 17 shows the stream lines at $t = 23000\tau_A$. The structure rotates in the poloidal direction corresponding to the large E^0_k. We also plot the total kinetic energy with the Fourier expansion of eq.(8) in Fig.16, which shows the result without the self-consistent poloidal flow. Comparison of the results with and without the self-consistent flow indicates that the effect of the $n = 0$ component growth to the behavior of the total kinetic energy is small in this case. Systematic analysis for the self-consistent

poloidal flow at higher beta value will be carried out in future.

6 Concluding Remarks

In the present study, the nonlinear behavior of the LHD plasma is analyzed based on the reduced MHD equations.

In Ref.[8], we showed that for $\beta_0 = 0.5\%$ and with parabolic profile the fluctuations are mild and saturate at low level. In the present analysis we have first considered initial equilibria with fixed pressure profile. In this case and for both $\beta_0 = 1.0\%$ and $\beta_0 = 1.5\%$ a bursting behavior is observed in the evolution of the kinetic energy. This bursting behavior is attributed to the overlapping of the vortices with different helicity. The vortices increase their size by merging each other in the radial direction. The pressure in the wide core region is transported outward in a short time by the convection of the large scale vortices. Therefore, the bursting activity may limit achievable beta.

On the other hand, the bursting activity can be suppressed by considering as initial conditions a sequence of equilibria with pressure profiles obtained from the nonlinear saturation of the instabilities at the lower beta value. This is due to the fact that the driving force at rational surfaces are reduced by the local flattening of the pressure profile, which is generated by the mild saturation at lower beta value. It was also shown that the radial width of the linear eigenfunction is reduced as the flat pressure region is enhanced at the resonant surface[13, 14, 15]. Thus, the vortices cannot overlap each other and the bursting activity is suppressed not only at $\beta_0 = 1.0\%$ but also at $\beta_0 = 1.5\%$. Consequently, the stabilizing mechanism in the LHD plasma is considered to be the continuous deformation of the pressure profile due to the nonlinear saturation of the interchange mode.

The linear stability improvement is also confirmed in the sequence of the saturated pressure profile. The Mercier quantity D_I becomes locally negative at the low order rational surfaces at $\beta_0 = 1.5\%$. The global pressure profile becomes broad as the beta value increases in this sequence. This tendency is consistent with the experimental data.

Even in the bursting case, the pressure profile is flattened locally in the saturation of the dominant linear mode. However, the flattening does not contribute to the stabilization of the following activity. The formation of local flat region increases the pressure gradient in the outside of the flat region. In the case of the smooth pressure profile such as eq.(1), the gradient

becomes quite steep. This is because the pressure gradient in the region is originally steep in the initial profile and the large driving force of the dominant linear mode results in the strong convection. Therefore, many modes grow abruptly in the region to cause the bursting activity. In the cases of the sequence of the pressure profile, the initial pressure profile with several local flat region reduces the driving force at the resonant surface of the dominant linear mode and the rational surfaces in the outside region.

In the present analysis, the viscosity and the heat conductivity are slightly increased at $\beta_0 = 1.0\%$ and 1.5%. This enhancement of the dissipation has a stabilizing effect on the linear mode. However, the bursting activity for the fixed pressure profile is not reduced by the increase of F_β in the range used here, because the behavior is quite similar to the result for $F_\beta = 1.0$ at $\beta_0 = 1.0\%$ obtained in Ref.[8]. This may be due to the fact that the vorticity overlap is enhanced by the broadening of the eigenfunction. On the other hand, in the sequence of pressure cases, we obtain weak bursting activities for F_β smaller than those used here, however, they are suppressed for the slight increase of F_β up to the values used here. This is because the sequence of pressure profile significantly reduces the driving force of the interchange modes. It follows that the local flattening of the pressure profile is the essential mechanism to suppress the bursting activity rather than the slight enhancement of the dissipation in the present study.

The effect of the finite Larmor radius (FLR) can also the interchange mode. Ref.[16] shows that the stabilizing effect to the linear mode is evident only in the marginally unstable case or the case of $D_I < 0.3$. (Note that the definition of D_I here[2] is different by 1/4 from that in Ref.[16].) However, in the case of the shifted-in LHD, D_I becomes easily beyond 0.3 even at small beta. as show in Fig.1. and Fig.14. Therefore, the FLR effect cannot be the main mechanism of the stabilization in the present case. In the nonlinear point of view, the region for local flattening of the pressure profile discussed here is more global than the radial width of the interchange mode that the FLR effect can stabilize. Hence, the direct effect of FLR to the generation of the local flattening structure in the pressure profile is small. However, the global flow due to the diamagnetic effect may change the nonlinear behavior. The systematic analysis for this point will be needed as discussed in Section 5.

The present study is the first step of the confirmation of the stabilizing mechanism attributed to the local pressure flattening in the increase of the beta value. The calculation for higher beta value is in the scope of our study in near future.

Unfortunately, the local flattening region in the pressure profile related to the nonlinear

evolution of the interchange mode has not been identified. It will be necessary to carry out the precise comparison between the nonlinear calculation and the experimental data.

Acknowledgments

One of the authors (K.I.) thanks Dr. S.Sakakibara, Dr.K.Y.Watanabe and Dr. H.Yamada for their discussion about the LHD experiments. This work was partially supported by the Grant-in-Aid for Scientific Research (C) 13680572 of the Ministry of Education, Culture, Sports, Science and Technology, Japan.

References

[1] Motojima, O., et al., "Recent Advance in LHD Experiment", 19th Fusion Energy Conf. Lyon, 2002, paper OV/1-6.

[2] Glasser,A.H., Greene,J.M., Johnson,J.L., Phys. Fluids **18** (1975) 875.

[3] Liang, Y., et al., Plasma Phys. Control. Fusion **44** (2002) 1383.

[4] Ichiguchi, K., et al., Nucl. Fusion **29** (1989) 2093.

[5] Ichiguchi, K., "Ideal and Resistive Stability of Free-Boundary LHD Equilibria" (Proc. 1999 Intl. Stellarator Workshop, Madison, 1999), CD-ROM file P2-4 (2000).

[6] Hirshman,S.P., van Rij,W.I., Merkel,P., Comp. Phys. Comm. **43** (1986) 143.

[7] Ichiguchi, K., et al., Nucl. Fusion **41** (2001) 181.

[8] Ichiguchi,K., et al., Nucl. Fusion **43** (2003) 1101.

[9] Carreras, B.A., et al., Phys. Fluids **30** (1987) 1388.

[10] Ichiguchi,K., J. Plasma Fusion Res. SERIES, **3** (2000) 576.

[11] Ichiguchi,K., Nakajima,N., Gardner,H.J., Nucl. Fusion **36** (1996) 1157.

[12] Sakakibara, S., et al., Plasma Phys. Control. Fusion **44** (2002) A217.

[13] Carreras, B.A., et al., Phys. Plasmas **8** (2001) 990.

[14] T.Tatsuno, et al., Nucl. Fusion **39** (1999) 1391.

[15] Ichiguchi,K., J. Plasma Fusion Res. SERIES, **2** (1999) 286.

[16] Gupta, S., et al., Phys. Plasmas **9** (2002) 3395.

Figure Captions

Fig.1 Contour of positive Mercier quantity D_I in the $(\rho, \langle\beta\rangle)$ plane. Thick solid line shows the contour of $D_I = 0$. The region encircled by the thick solid line is unstable region. The thin solid lines in the unstable region are contour of D_I differing by $\Delta D_I = 0.2$. Dashed lines indicate the positions of the rational surfaces corresponding to $\iota = 2/5$, 3/7, 1/2, 3/5, 2/3 and 1.

Fig.2 Linear growth rates versus toroidal mode number n. Circles, triangles and squares show the growth rates for the pressure of eq.(1) at $\beta_0 = 0.5\%$, 1.0% and 1.5%, respectively. Numbers indicate the dominant poloidal mode number of each n mode.

Fig.3 Plot of (m, n) harmonics used in the nonlinear calculations.

Fig.4 Time evolution of the kinetic energy of the perturbation for the $\beta_0 = 1.0\%$ equilibrium with the pressure of eq.(1). Thick line shows the total energy and thin lines show the n=0, 1, 2, 3, 4, 5, 6 and 7 components.

Fig.5 Stream lines on the (ρ, θ) plane at $\zeta = 0$ cross section for the $\beta_0 = 1.0\%$ equilibrium at (a) $t = 4300\tau_A$, (b) $t = 4400\tau_A$ and (c) $t = 4620\tau_A$ with the pressure eq.(1), plotted only in the region of $\rho \leq 0.8$. Different thickness of the lines means the different polarization of the flow.

Fig.6 Profiles of average pressure $\langle P\rangle$ (solid lines) at $t = 0$, $6500\tau_A$, and $27000\tau_A$ and average rotational transform $\langle\iota\rangle$ (dashed line) at $t = 27000$ in the region of $\rho \leq 0.8$ for the $\beta_0 = 1.0\%$ equilibrium with the pressure eq.(1). Several rational surfaces are indicated.

Fig.7 Profiles of average pressure $\langle P\rangle$ (solid lines) at $t = 0$, $21500\tau_A$, and $27000\tau_A$ and average rotational transform $\langle\iota\rangle$ (dashed lines) at $t = 27000$ in the region of $\rho \leq 0.8$ for the $\beta_0 = 1.0\%$ equilibrium with the saturated pressure profile at $\beta_0 = 0.5\%$. Profile of the average pressure at $t = 27000\tau_A$ in Fig.6 is also shown by dotted line for the comparison.

Fig.8 Linear growth rates versus toroidal mode number n for the $\beta_0 = 1.0\%$ equilibria with the pressure profile of eq.(1) (triangles) and the saturated pressure profile at $\beta_0 = 0.5\%$ (squares). Numbers indicate the dominant poloidal mode number of each n mode.

Fig.9 Time evolution of the kinetic energy of the perturbation for the $\beta_0 = 1.0\%$ equilibrium with the saturated pressure profile at $\beta_0 = 0.5\%$. Thick line shows the total energy and thin lines show the $n = 0$, 1, 2, 3, 4, 5, 6 and 7 components.

Fig.10 Stream lines on the (ρ, θ) plane at $\zeta = 0$ cross section for the $\beta_0 = 1.0\%$ equilibrium at $t = 21500\tau_A$ with the saturated pressure profile at $\beta_0 = 0.5\%$, plotted only in the region of $\rho \leq 0.8$. Different thickness of the lines means the different polarization of the flow.

Fig.11 Time evolution of the kinetic energy of the perturbation for the $\beta_0 = 1.5\%$ equilibrium with the saturated pressure profile at $\beta_0 = 1.0\%$. Thick line shows the total energy and thin lines show the $n = 0$, 1, 2, 3, 4, 5, 6 and 7 components. Time evolution of the total kinetic energy for the $\beta_0 = 1.5\%$ equilibrium with the pressure of eq.(1) is also plotted for the comparison.

Fig.12 Pressure contour on the (ρ, θ) plane at $\zeta = 0$ cross section for the $\beta_0 = 1.5\%$ equilibrium at $t = 27000\tau_A$ with the saturated pressure profile at $\beta_0 = 1.0\%$, plotted only in the region of $\rho \leq 0.8$.

Fig.13 Profiles of average pressure $\langle P \rangle$ (solid lines) saturated at $\beta_0 = 0.5\%$, 1.0% and 1.5% with the profile of eq.(1), and average rotational transform $\langle \iota \rangle$ at 1.5% (dashed line).

Fig.14 Profiles of Mercier quantity D_I for pressure profile of eq.(1) (dashed lines) and the saturated pressure profiles (solid lines) at $\beta_0 = 0.5\%$ (thin) and 1.5% (thick). Numbers denote the values of the rotational transform at the positions.

Fig.15 Peaking parameter of pressure profile observed in experiments[12] (open circles) and obtained by the nonlinear calculation (closed circles).

Fig.16 Time evolution of the kinetic energy of the perturbation for the $\beta_0 = 0.5\%$ equilibrium with the pressure profile of eq.(1) including self-consistent flow. Thick line shows the total energy and thin lines show the $n = 0$, 1, 2, 3, 4, 5, 6 and 7 components. Dashed line shows time evolution of the total kinetic energy without self-consistent flow.

Fig.17 Stream lines on the (ρ, θ) plane at $\zeta = 0$ cross section at $t = 23000\tau_A$ for the $\beta_0 = 0.5\%$ equilibrium with the pressure profile of eq.(1) including self-consistent flow, plotted only in the region of $\rho \leq 0.8$.

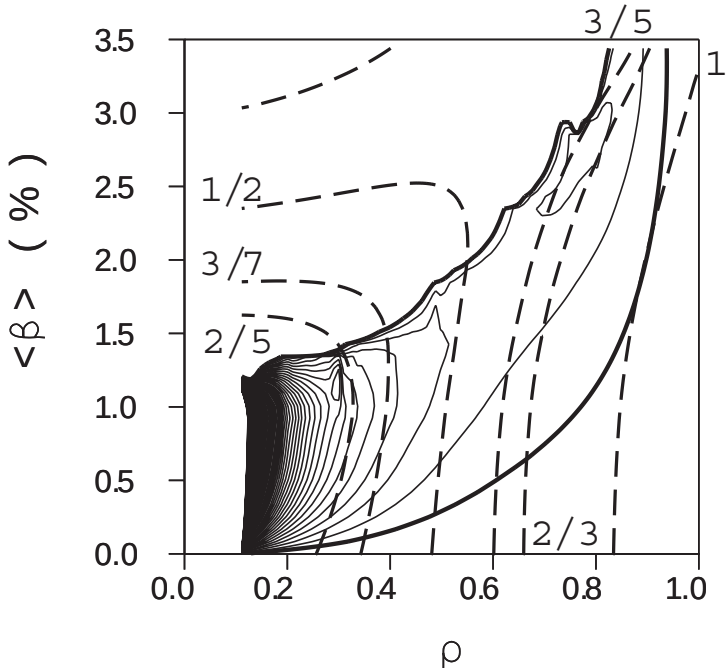
3/5
1
1/2
3/7
2/5
2/3
3.5
3.0
2.5
2.0
1.5
1.0
0.5
0.0
<β> (%)
0.0
0.2
0.4
0.6
0.8
1.0
ρ

FIG.1.

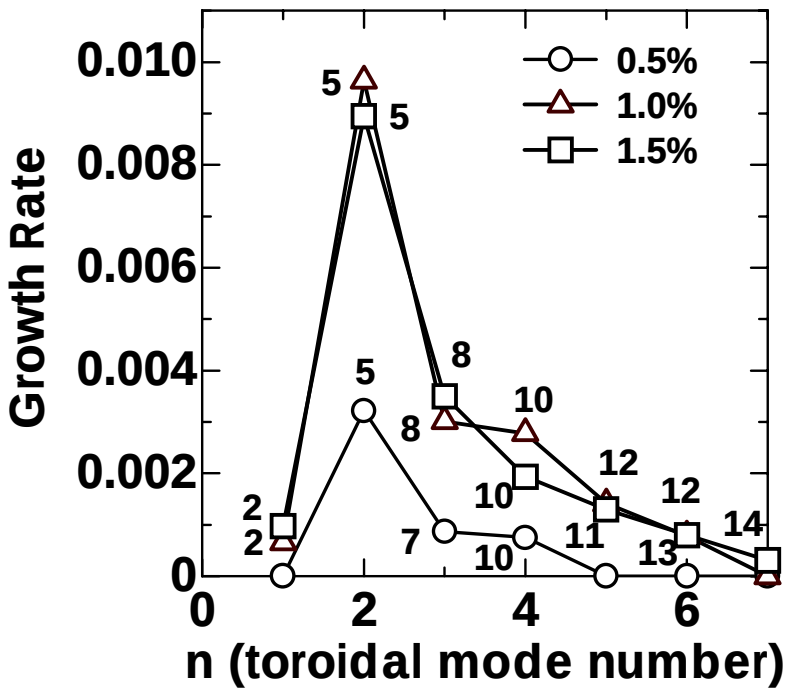
0.5%
1.0%
1.5%
Growth Rate
0.010
0.008
0.006
0.004
0.002
0
0
2
4
6
n (toroidal mode number)

FIG.2.

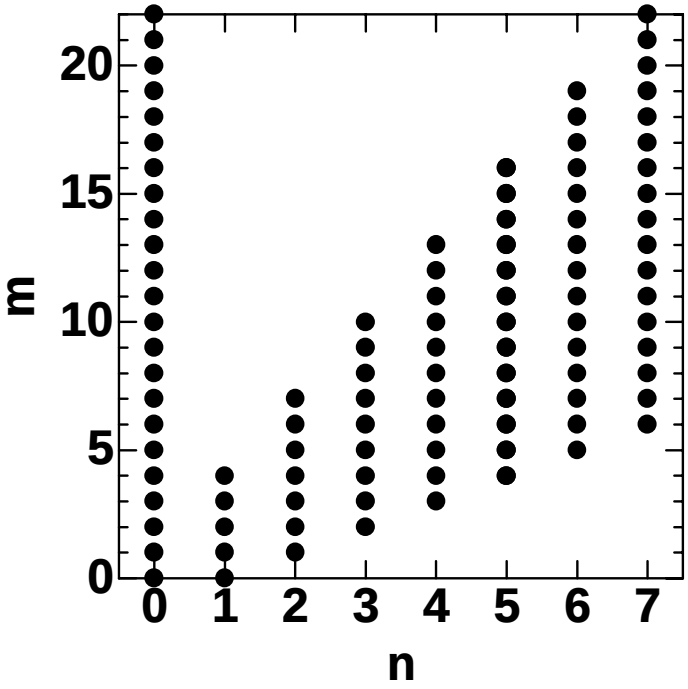
m
n
0
5
10
15
20
0
1
2
3
4
5
6
7

FIG.3.

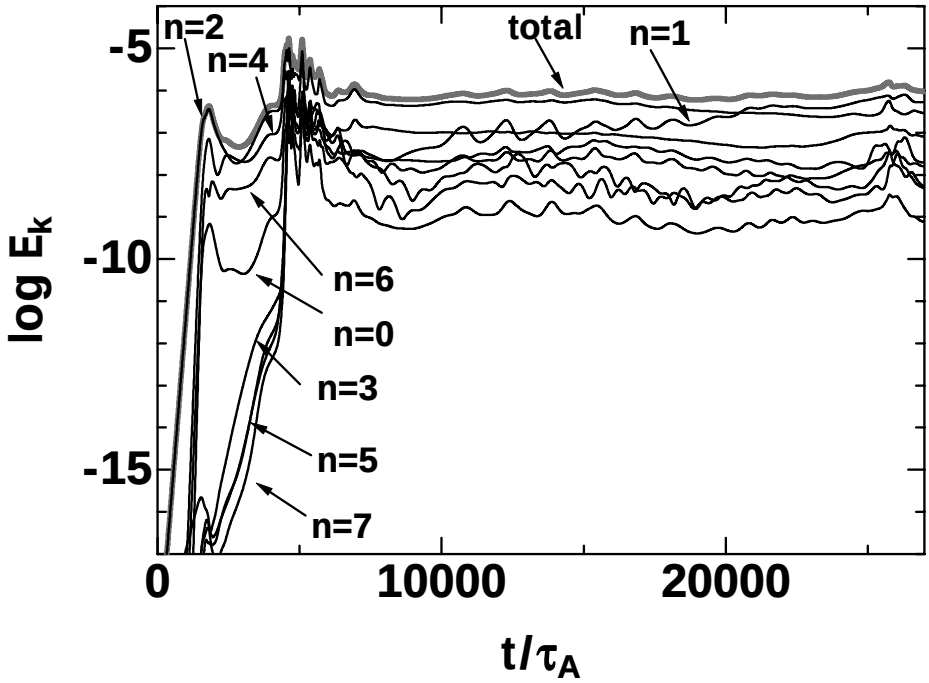
log E_k
t/τ_A
-5
-10
-15
0
10000
20000
n=2
n=4
total
n=1
n=6
n=0
n=3
n=5
n=7

FIG.4.

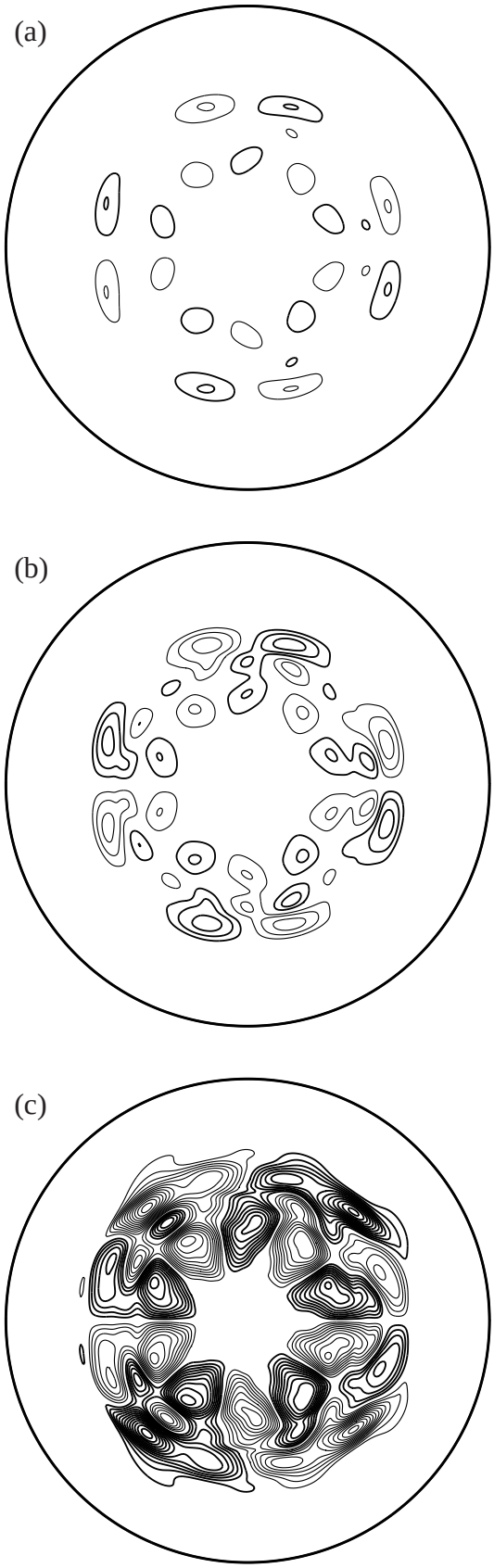

FIG.5.

‘ MHD Analysis of LHD High Beta Plasma’, K.Ichiguchi, N.Nakajima, B.A.Carreras

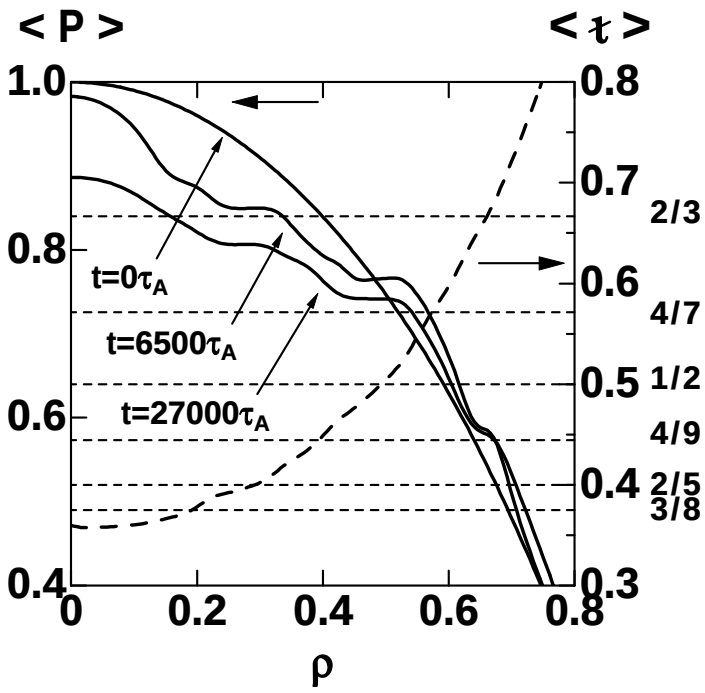
< P >
< ι >
1.0
0.8
0.6
0.4
0.8
0.7
0.6
0.5
0.4
0.3
2/3
4/7
1/2
4/9
2/5
3/8
t=0τA
t=6500τA
t=27000τA
0
0.2
0.4
0.6
0.8
ρ

FIG.6.

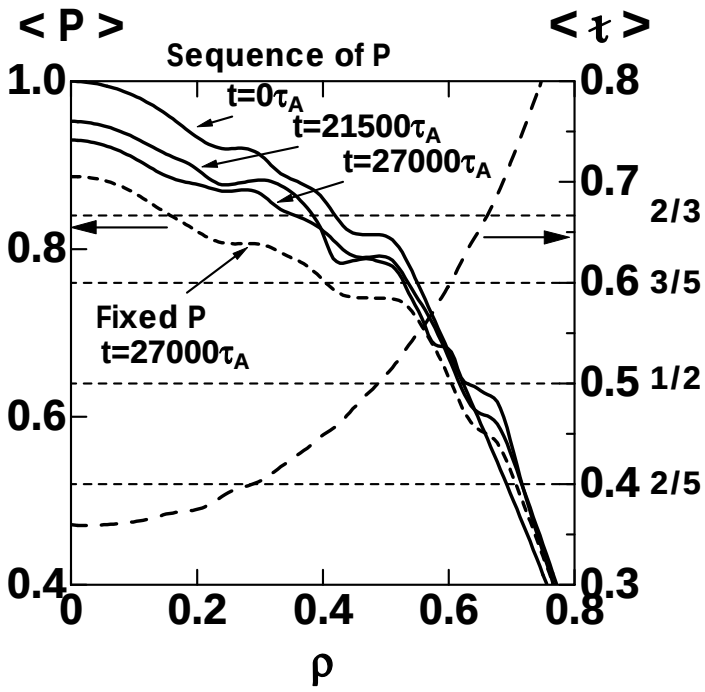
< P >
< ι >
Sequence of P
1.0
0.8
0.6
0.4
0.8
0.7
0.6
0.5
0.4
0.3
2/3
3/5
1/2
2/5
t=0τA
t=21500τA
t=27000τA
Fixed P
t=27000τA
0
0.2
0.4
0.6
0.8
ρ

FIG.7.

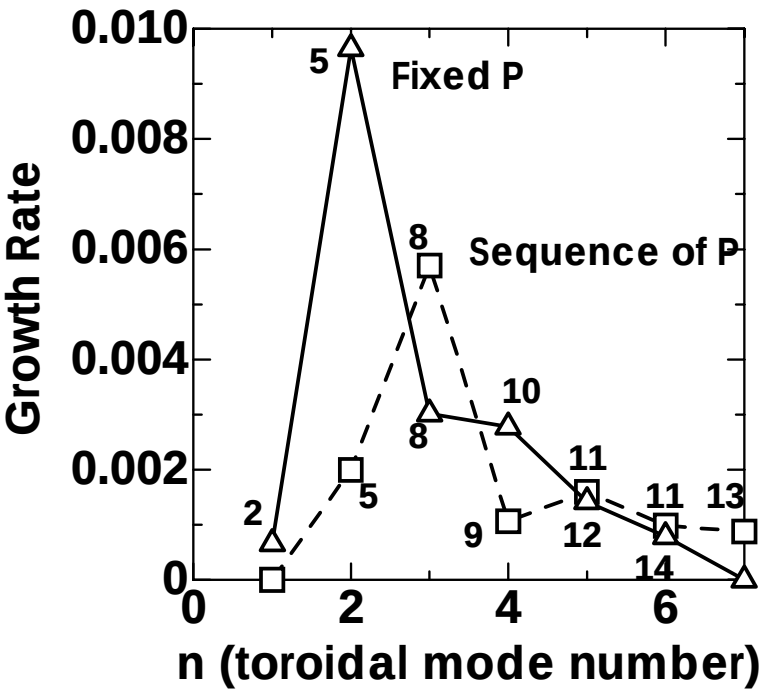
0.010
0.008
0.006
0.004
0.002
0
Growth Rate
Fixed P
Sequence of P
5
8
10
8
11
2
5
11
13
9
12
14
0
2
4
6
n (toroidal mode number)

FIG.8.

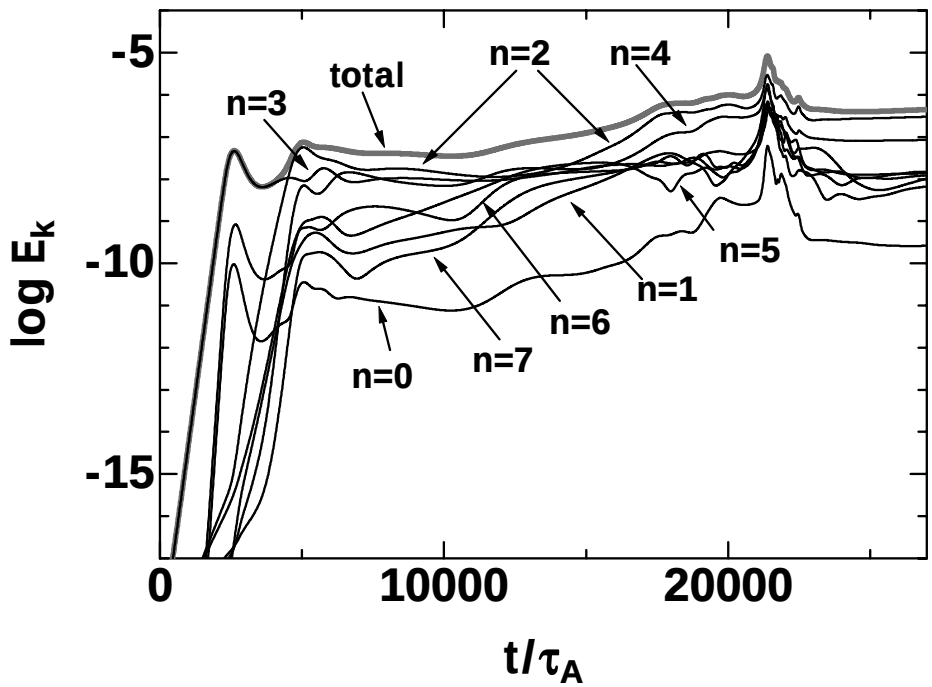
-5
-10
-15
log E_k
total
n=2
n=4
n=3
n=5
n=1
n=6
n=7
n=0
0
10000
20000
t/τ_A

FIG.9.

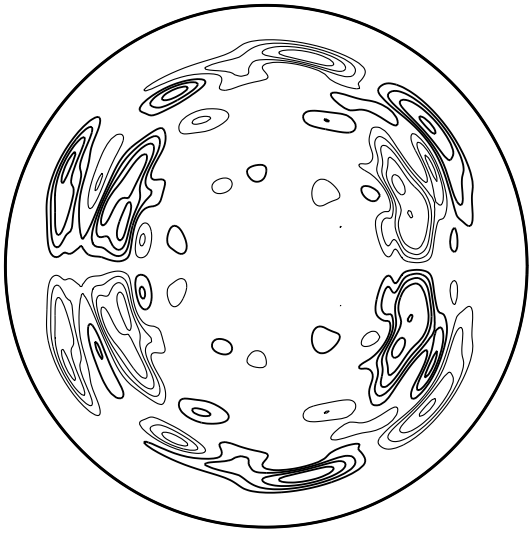

FIG.10.

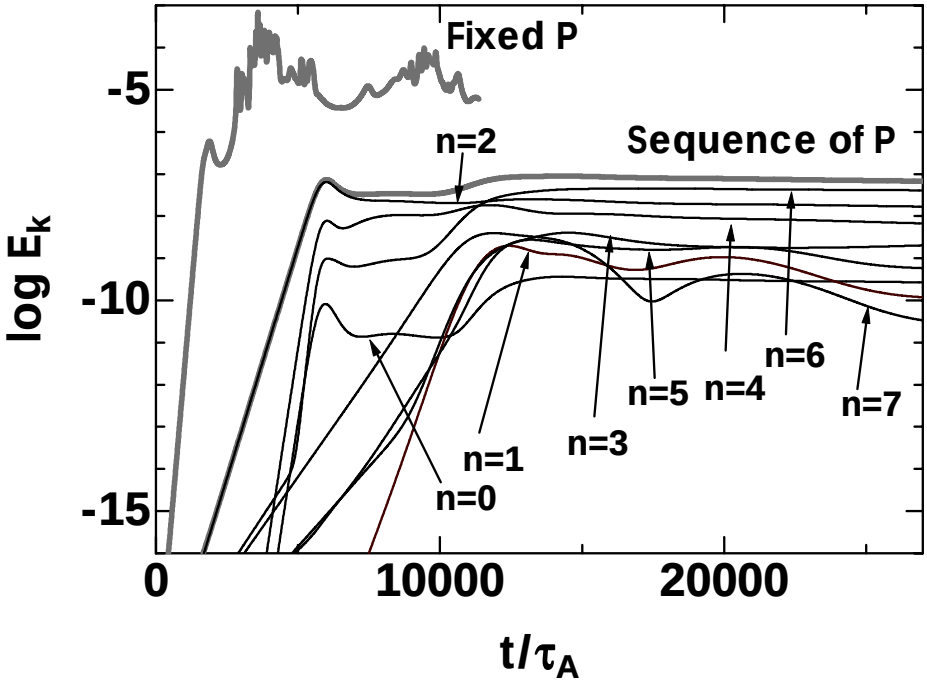
Fixed P
Sequence of P
n=2
n=0
n=1
n=3
n=5
n=4
n=6
n=7
-5
-10
-15
0
10000
20000
log E_k
t/τ_A

FIG.11.

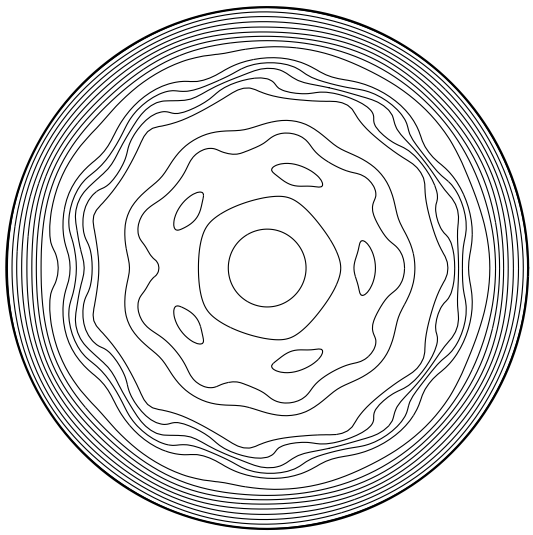

FIG.12.

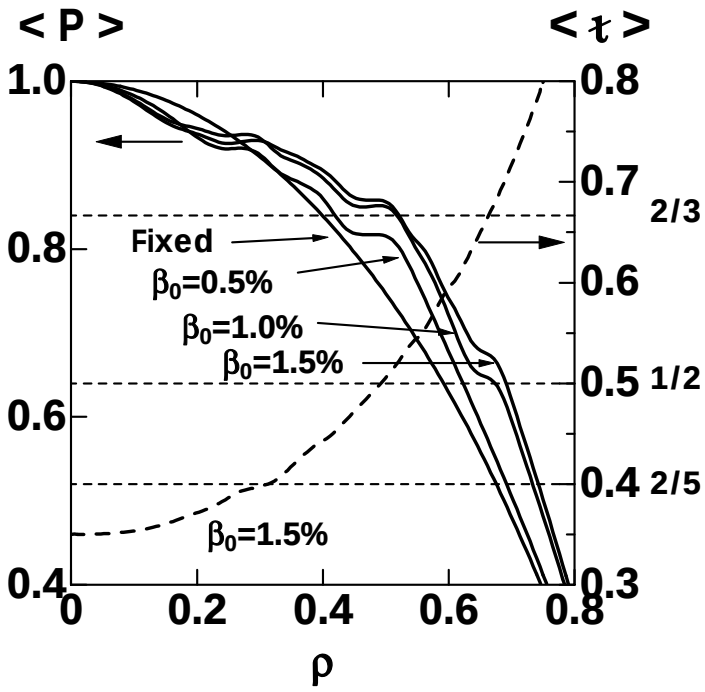
< P >
< ι >
1.0
0.8
0.6
0.4
0.8
0.7
0.6
0.5
0.4
0.3
2/3
1/2
2/5
Fixed
β0=0.5%
β0=1.0%
β0=1.5%
β0=1.5%
0
0.2
0.4
0.6
0.8
ρ

FIG.13.

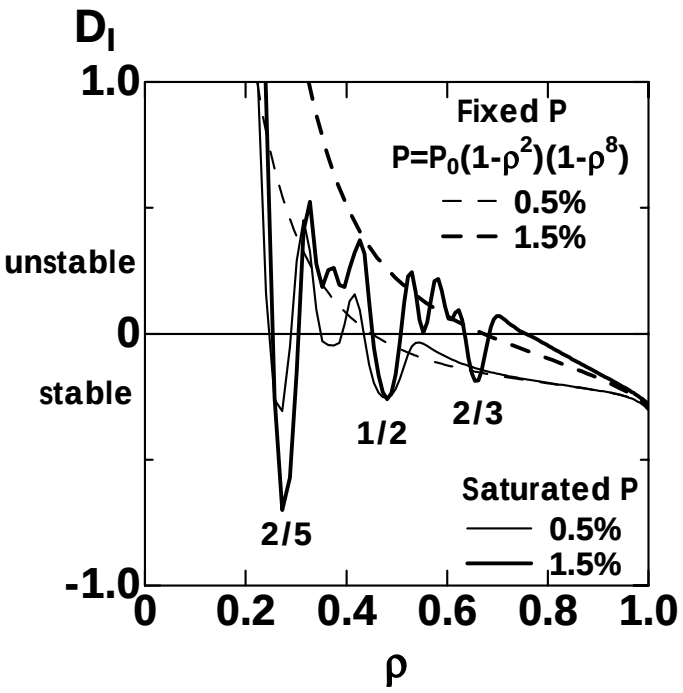
D_I
1.0
unstable
0
stable
-1.0
Fixed P
$P=P_0(1-\rho^2)(1-\rho^8)$
0.5%
1.5%
2/5
1/2
2/3
Saturated P
0.5%
1.5%
0
0.2
0.4
0.6
0.8
1.0
ρ

FIG.14.

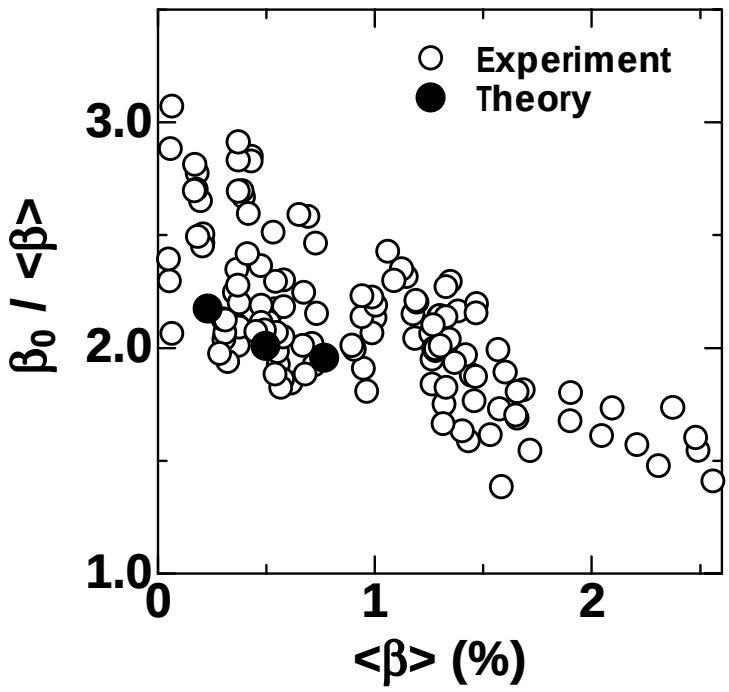
Experiment
Theory
3.0
2.0
1.0
β_0 / <β>
0
1
2
<β> (%)

FIG.15.

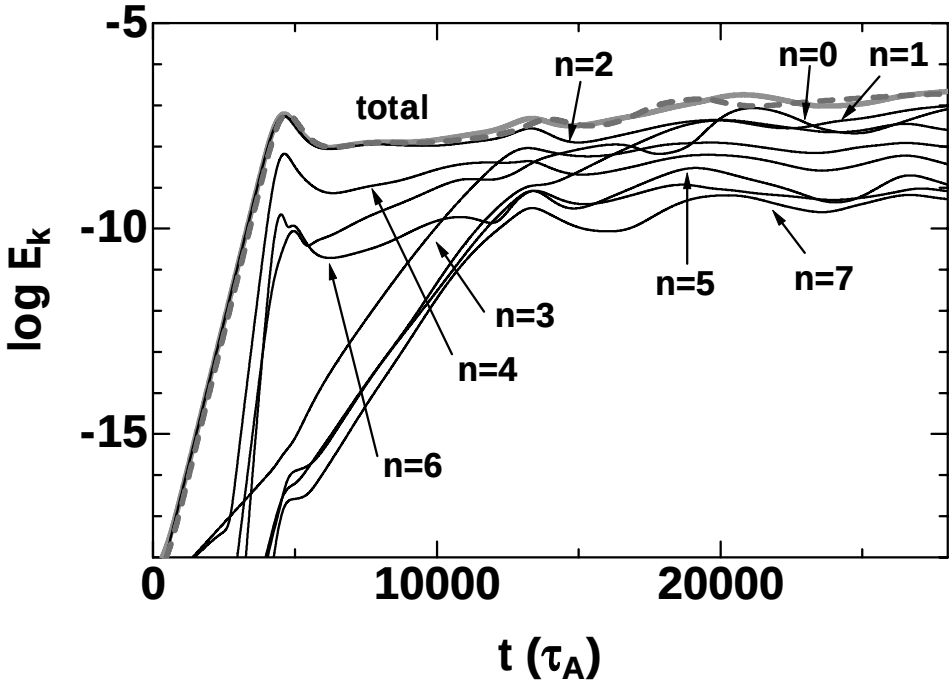

FIG.16.

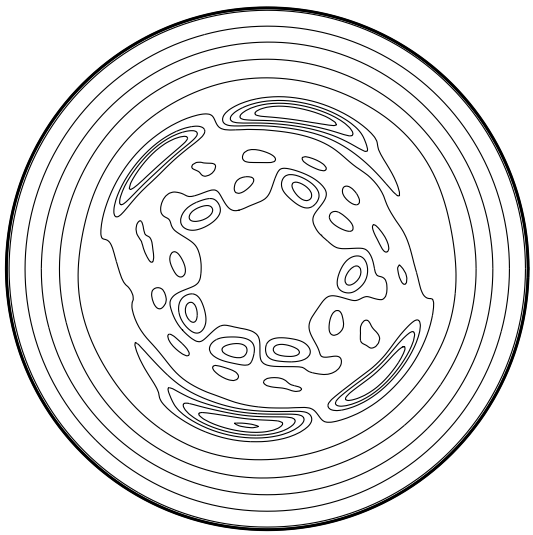

FIG.17.